



저작자표시-비영리-동일조건변경허락 2.0 대한민국

이용자는 아래의 조건을 따르는 경우에 한하여 자유롭게

- 이 저작물을 복제, 배포, 전송, 전시, 공연 및 방송할 수 있습니다.
- 이차적 저작물을 작성할 수 있습니다.

다음과 같은 조건을 따라야 합니다:



저작자표시. 귀하는 원저작자를 표시하여야 합니다.



비영리. 귀하는 이 저작물을 영리 목적으로 이용할 수 없습니다.



동일조건변경허락. 귀하가 이 저작물을 개작, 변형 또는 가공했을 경우에는, 이 저작물과 동일한 이용허락조건하에서만 배포할 수 있습니다.

- 귀하는, 이 저작물의 재이용이나 배포의 경우, 이 저작물에 적용된 이용허락조건을 명확하게 나타내어야 합니다.
- 저작권자로부터 별도의 허가를 받으면 이러한 조건들은 적용되지 않습니다.

저작권법에 따른 이용자의 권리는 위의 내용에 의하여 영향을 받지 않습니다.

이것은 [이용허락규약\(Legal Code\)](#)을 이해하기 쉽게 요약한 것입니다.

[Disclaimer](#)

Master's Thesis

Abstract

Rational Catalyst Design for Clean Energy Conversion

Zheng, Yongping

School of Mechanical and Aerospace Engineering

WCU Multiscale Mechanical Design

Seoul National University

Biomimetic non-precious-metal catalysts based on metal-porphyrin-like (FeN_4 , CoN_4) moieties have been shown competitive with platinum-based catalysts for oxygen reduction reaction (ORR) in fuel cells. However, the exact nature of the active sites in these materials is still not clearly understood, which prevents us from further optimization design. Here we report a first principles study of these metal-nitrogen-carbon materials with varied combinations of M, N, C (M=Mn, Fe, Co, Ni). By calculating the intermediate electrochemical steps in ORR process, each involving one electron transfer, we found that the square-pyramid FeN_4 -Pyrrole (FeN_5) or square-planar CoN_4 moieties incorporated graphenes have the best

performance in terms of both catalytic activity and chemical stability. Although square-planar NiC_4 and square-pyramid CoC_2N_2 -Pyrrole (CoC_2N_3) also show good activity, carbon sites adjacent to the metal atom can be easily attacked by active oxygen and leading to severe degradation. We also found that the carbon sites adjacent to nitrogen atoms are mostly responsible for H_2O_2 production, and they are more vulnerable than the nitrogen atoms towards oxidization to cause dissociation of active moieties and degradation.

Keywords: DFT, PEMFC, non-precious-metal catalyst, biomimetic, graphene

Student Number: 2013-22500

Contents

Abstract	i
Nomenclatures	iv
List of Figures	v
Chapter 1 Introduction	1
Chapter 2 Methodology	2
2.1 Computational Methods	2
2.2 Binding Energy Definition	3
2.3 Electrochemical Definition	4
Chapter 3 Result and Discussion	5
3.1 Initial Screening	5
3.2 Electrochemical Calculation	7
3.3 Degradation Analysis	12
Chapter 4 Conclusion	14
Bibliography	15
초 록	18

Nomenclatures

U	Cell potential applied on the half cell
ΔG	Reaction energy of a specific reaction
n	Electron transfer during a reaction
e	One electron charge $1.6021765 \times 10^{-19}$ coulomb
ORR	Oxygen reduction reaction
PEMFC	Polymer electrolyte membrane fuel cell
DFT	Density function theory
U_1	Highest cell potential that all the four electron reduction steps are downhill
U_2	Lowest cell potential that all the two electron reduction steps are uphill

List of Figures

Figure 1 O binding energies on different moieties. The upper dash line denotes the O binding energy on a nitrogen doped graphene; the under one is the maximum O binding energy on a Pt (111) surface.

Figure 2 Free-energy diagram for ORR process over FeN₄ and CoN₄ incorporated graphene. Here, * denotes a catalytic site; $U=0$ denotes the zero cell potential, corresponding to the reaction run-ning by short circuiting the cell; $U=0.34$ V is the highest cell poten-tial where all reaction steps on FeN₄ moiety are downhill, while $U=0.64$ V is that on CoN₄.

Figure 3 U_1 and U_2 values on different square-planar active centers plotted as a function of the oxygen binding energy, where U_1 value is the highest cell potential defined in **Fig. 2** for four-electron reduction and U_2 for two-electron reduction, a high U_1 value and a low U_2 value is desirable for an efficient ORR catalyst. The U values on platinum (111) surface is shown as reference, and the dash line is a guide of eye to show the common onset cell potential of fuel cells.

Figure 4 Pyrrole radical binding energy on four-coordination active centers is defined in Reaction 3, with unpaired nitrogen bonded with the metal center. More negative binding energy indicate stronger tendency to form five-coordination square-pyramid structure.

Figure 5 U_1 and U_2 values of ORR process on all possible square-pyramid metal centers are plotted as a function of O binding energy, yielding a high activity plateau region versus a moderate binding energy around 0 eV.

Figure 6 Undesirable O binding configuration on the carbon surrounded active center and leads to possible degradation.

Chapter 1 Introduction

Biomimetic design is an eternal topic in diverse areas due to miracle bio-functions, resulting from long-term evolution, in the living organisms. In the development of fuel cells, devices that directly convert the chemical energy of a fuel into electricity, superior non-precious-metal oxygen-reduction catalysts design turns out to be the crux. In the living biological cells, enzymes are highly selective and efficient molecule catalysts, responsible for thousands of metabolic processes including redox reactions, therefore to understand the underlying active factors of biocatalysts for redox reactions may be a potential solution to the catalyst design issue for fuel cells.

Since 1964, when cobalt phthalocyanine was first observed to catalyze the ORR by Jasinski,¹ a class of organic compounds, metal porphyrins have received increasing attention, among which cobalt and iron porphyrins are regarded as the most promising precursors. Through decades of efforts, this metal-nitrogen-carbon (M-N-C, M=Fe, Co) type of materials have achieved quite good performance in fuel cells, rivaling state-of-the-art platinum-based catalysts,²⁻⁴ especially for the recent low dimensional materials, FeN₄ or CoN₄ incorporated carbon nanotube and graphene.⁵⁻⁹ Though the FeN₄ or CoN₄ moieties are commonly viewed as the active ORR sites, theoretical understanding of their catalytic nature, and further optimization strategy are remaining unknown. In this work, we applied density function theory (DFT)

simulations to this kind of materials to explore the underlying catalytic essence.

On the cathode in fuel cells, especially for polymer electrolyte membrane fuel cells (PEMFCs), O_2 can be reduced following two paths. One is so-called '4e⁻ reduction' in which O_2 is completely reduced to two H_2O via 4 electrons transfer, and it is desired for the high efficient energy conversion. The other is called '2e⁻ reduction' in which H_2O_2 is produced via 2 electrons transfer, resulting in lower power density and severe chemical degradation. Therefore, selective catalysts that can accelerate the 4e⁻ reduction and inhibit the 2e⁻ reduction is demanded. Earlier studies by Norskov suggested that the ORR activity on metal surfaces is a trade-off between not too strong and not too weak O binding energies, and it can be described as a function of O binding energies, which yields a volcano curve.¹⁰ A too weak O binding catalyst usually has difficulty in formation of OOH intermediate on the surface, while a too strong O binding one is mostly rate determined by the removal of OH intermediate.¹¹⁻¹³

Chapter 2 Methodology

2.1 Computational Methods

Density functional theory (DFT) calculations are carried out to study the graphene based catalyst materials. The system energy calculations are performed by using the Vienna *ab initio* simulation package (VASP) code.¹⁴⁻¹⁷ The projector augmented wave (PAW) method^{18,19} is used to describe the

ionic potential and the Perdew-Burke-Ernzerhof (PBE) functional^{20,21} is used to describe the exchange correlation interactions. The plane-wave kinetic energy cutoff is 400 eV, and a $6 \times 6 \times 1$ Monkhorst k -point mesh is used for the Brillouin zone sampling in all the calculations. For structure relaxation, the energy convergence criterion for electronic relaxation is 1×10^{-4} eV, and the ionic relaxation is performed until all forces are smaller than 0.005 eV/Å. The conjugate gradient method is used to minimize the Hellmann–Feynman forces in the ionic relaxations.

2.2 Binding Energy Definition

In this work, the mentioned oxygen adsorption energies are calculated with respect to oxygen in the gas phase, as the reaction energies of the following reactions



Where O_2 is in the gas phase, $*$ denotes an adsorption site, O_2^* and O^* are the adsorbed oxygen molecule and atom, respectively. While, the mentioned Pyrrole radical binding energy in the later part of this work is defined as the reaction energy of the following reaction,



A negative binding energy shows an exothermic reaction, indicating a

thermodynamically favorable tendency of binding another ligand in one side of the active center forming square-pyramid structure.

2.3 Electrochemical Definition

To investigate the electrochemical reactions, the following equation is used to determine the theoretical potential

$$\Delta G = -neU \quad (\text{Equation 1})$$

Here, ΔG is the free energy of a reaction, n is the number of electrons involved, and U is the potential. In hydrogen fuel cells, the calculated equilibrium potential is determined by the reaction



Where the $(\text{H}^+ + \text{e}^-)$ couple is in equilibrium with gas phase H_2 , i.e., the free energy of $G(\text{H}^+ + \text{e}^-) = 1/2G(\text{H}_2)$. Both the oxygen and water molecule are in the gas phase. Thus, we can get the theoretical equilibrium potential according to (Eqn.1) versus standard hydrogen electrode, $U_0 = -\Delta G/4e = 1.26 \text{ V}$, close to the standard value 1.23 V.

Chapter 3 Result and Discussion

3.1 Initial Screening

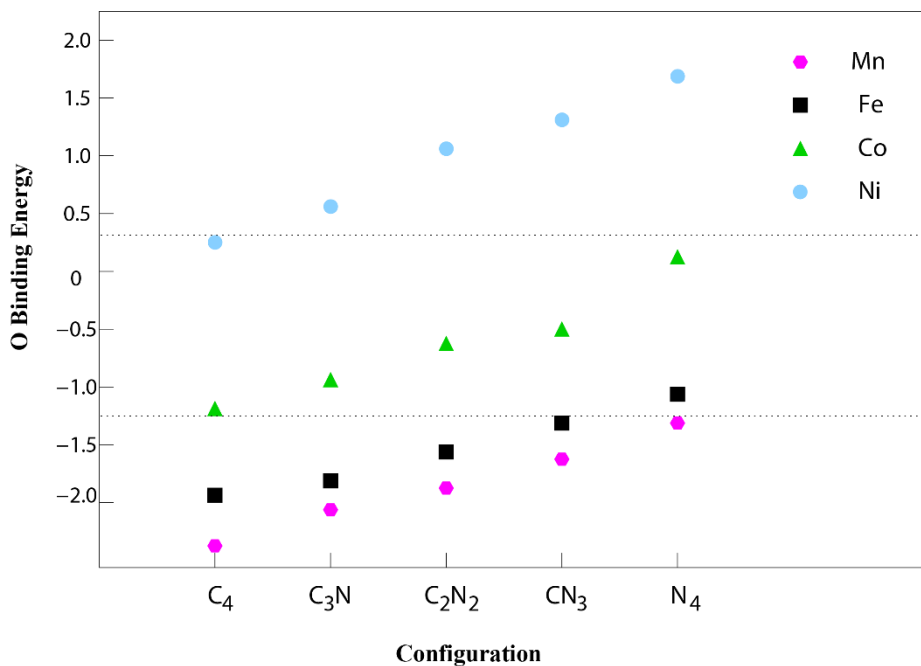


Figure 1 O binding energies on different moieties. The upper dash line denotes the O binding energy on a nitrogen doped graphene; the under one is the maximum O binding energy on a Pt (111) surface.

According to this understanding, an initial catalytic activity screening among various MC_xN_y ($M=Mn, Fe, Co, Ni, x+y=4$) moieties is proceeded by calculating their O binding energies. In Figure 1, O binding energies on different MC_xN_y moieties are calculated with respect to O_2 in gas phase (Reaction 2), and two benchmarks are adopted to distinguish a feasible binding energy region that is moderate for ORR catalysis. One is the maximum O binding energy on platinum (111) surface as the strong binding

limit, reasoning that Pt (111) was shown to locate at the strong binding region but most close to the peak of ORR volcano curve.¹⁰ Actually, the O binding energy on Pt (111) varies in a wide range, sensitive to different adsorption sites and oxygen coverage, and the maximum O binding energy is obtained on the hollow site under low oxygen coverage, about -1.32 eV, consistent with the previous DFT work.²² The other one is the O binding energy on a carbon site adjacent to the nitrogen dopant in a N-doped graphene as the weak binding limit, since N-doped graphenes have been reported active in ORR catalysis,^{23,24} but our previous work has pointed that N-doped graphene is still too weak towards O adsorption, about 0.34 eV.²⁵

Based on these two benchmarks, we can find that both FeN₄ and CoN₄ are in the feasible region for ORR catalysis, but each close to opposite limits. To dig out the underlying difference, detailed electrochemical reactions are investigated on these moieties. In Figure 2, free-energy diagram of ORR processes over FeN₄ and CoN₄ moieties is shown to illustrate the catalytic nature and difference between strong-binding and weak-binding materials.

3.2 Electrochemical Calculation

In this diagram, ORR process is simulated by calculating five elementary steps. As we can see from Figure 2, the initial reaction is adsorption of molecule O₂, and the others are four electrochemical reactions involving one electron transfer each step, which are sensitive to applied cell potential, by shifting each reaction energy with eU . Here, both ‘2e⁻’ and ‘4e⁻’ reduction routes are depicted to demonstrate two crucial factors that describe an ORR

catalyst, ‘2e⁻ reduction’ inhibiting ability and ‘4e⁻ reduction’ catalytic ability. On FeN₄, who is close to the strong binding limit, we find that the removal of

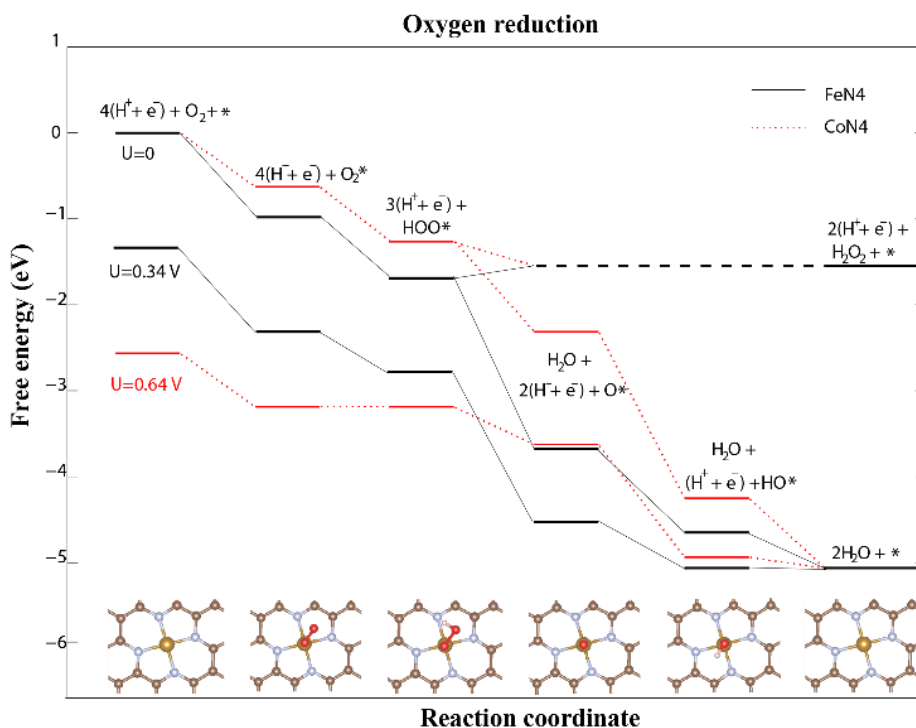


Figure 2 Free-energy diagram for ORR process over FeN₄ and CoN₄ incorporated graphene. Here, * denotes a catalytic site; $U=0$ denotes the zero cell potential, corresponding to the reaction run-ning by short circuiting the cell; $U=0.34$ V is the highest cell poten-tial where all reaction steps on FeN₄ moiety are downhill, while $U=0.64$ V is that on CoN₄.

adsorbed OOH intermediate to form H₂O₂ is uphill by 0.22 eV under zero cell potential, which means the ‘2e⁻ reduction’ is well inhibited with at least a 0.22 eV reaction barrier; however, due to the strong binding, adsorbed OH intermediate is also not so easy to be removed to produce H₂O, resulting that when cell potential U is more than 0.34 V, this final electrochemical step becomes uphill, therefore slow down the whole reaction kinetics and rate-

determine the overall '4e⁻ reduction'. While on CoN₄, who is close to the weak limit, we obtain a downhill value, -0.25 eV, to form H₂O₂ from adsorbed OOH intermediate under a zero cell potential, which means the removal of OOH becomes easier compared with that on FeN₄. Meanwhile, $U=0.64$ V is achieved where electron/proton- transfer step, formation of OOH intermediate from adsorbed molecule O₂, is beginning to become uphill. Consequently, catalysts that approaching the strong-binding limit is rate-determined by the removal of adsorbed OH, and has a good H₂O₂ inhibiting ability; while that approaching the weak-binding limit is rate-determined by the formation of OOH, and relatively poorer H₂O₂ inhibiting ability. Subsequently, we develop two parameters to describe the catalytic activity, U_1 , the highest cell potential where all reaction steps are downhill in the 4e⁻ reduction path; U_2 , the highest cell potential where all reaction steps are downhill in the 2e⁻ reduction path. So, high U_1 value and low U_2 value are desirable for an efficient ORR catalyst in fuel cells.

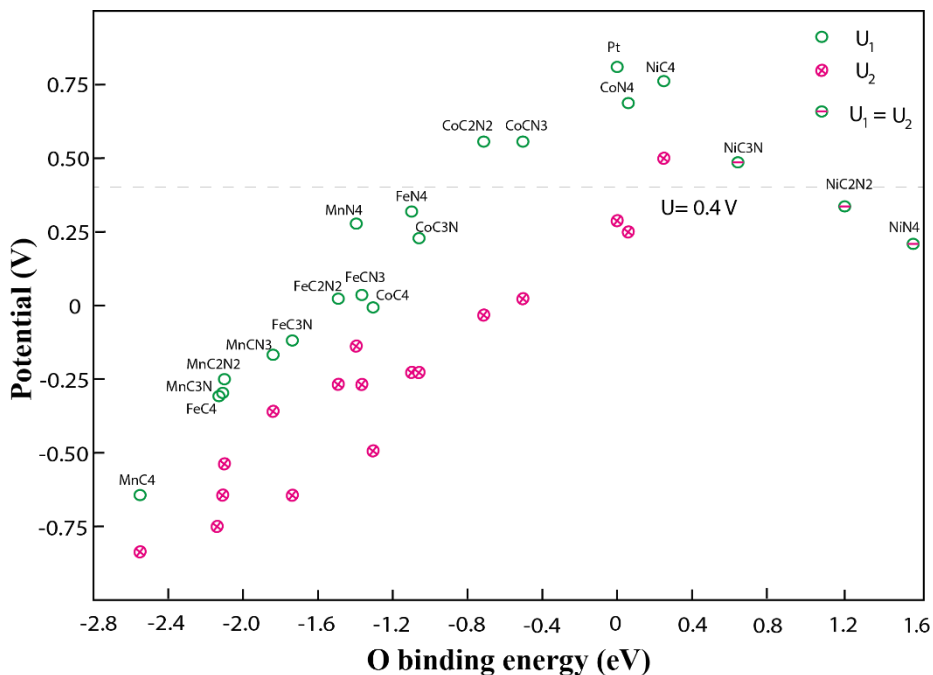


Figure 3 U_1 and U_2 values on different square-planar active centers plotted as a function of the oxygen binding energy, where U_1 value is the highest cell potential defined in Fig. 2 for four-electron reduction and U_2 for two-electron reduction, a high U_1 value and a low U_2 value is desirable for an efficient ORR catalyst. The U values on platinum (111) surface is shown as reference, and the dash line is a guide of eye to show the common onset cell potential of fuel cells.

In Figure 3, U_1 and U_2 values over varied moieties are calculated, and each plotted as a function of the O binding energy, yielding two volcano curves. We can find that the two volcano curves share the same right hillside on the weak-binding region, reasoning that both of them is rate-determined by the OOH formation step on this region, consistent well with the previous analysis. While the left hillsides of U_1 and U_2 are determined by the removal of OH and OOH intermediates steps, respectively. This plot also shows that among all four-coordination square-planar moieties, MC_xN_y ($x+y=4$), NiC₄ has the highest U_1 value, but also the highest U_2 values, which means poor inhibiting

ability of H₂O₂ production; CoN₄ has the second highest U_1 value and a much lower U_2 value, benefiting for ORR catalysis in fuel cells; others are mostly both lower U_1 and U_2 values because of the strong binding intermediates, besides the rest of Ni-based moieties are too weak to form OOH intermediate.

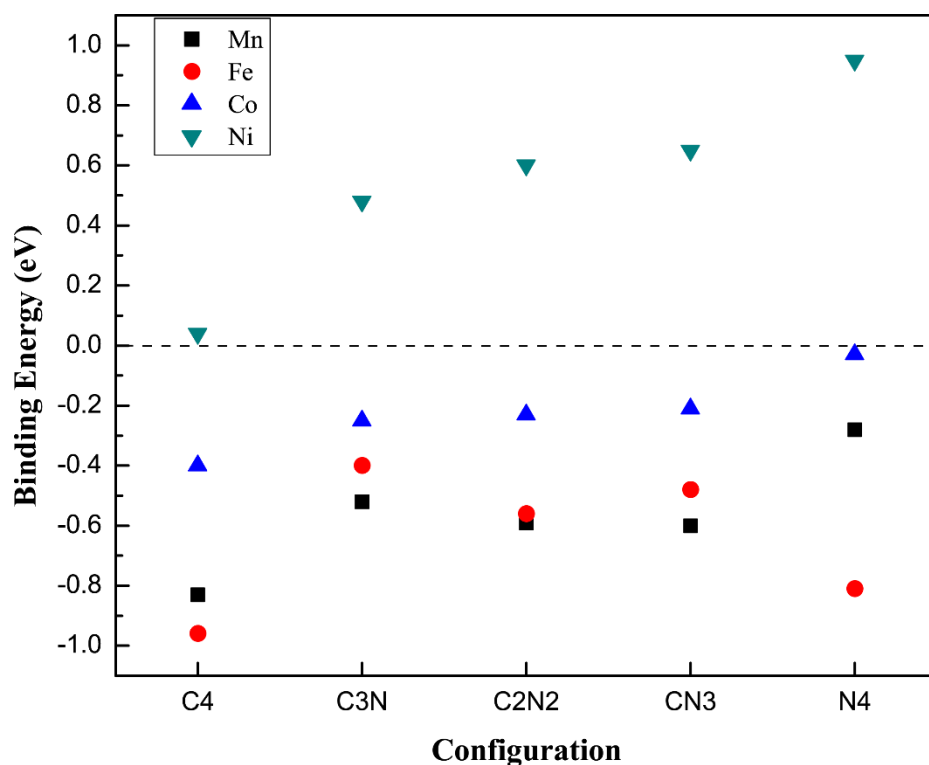


Figure 4 Pyrrole radical binding energy on four-coordination active centers is defined in Reaction 3, with unpaired nitrogen bonded with the metal center. More negative binding energy indicate stronger tendency to form five-coordination square-pyramid structure.

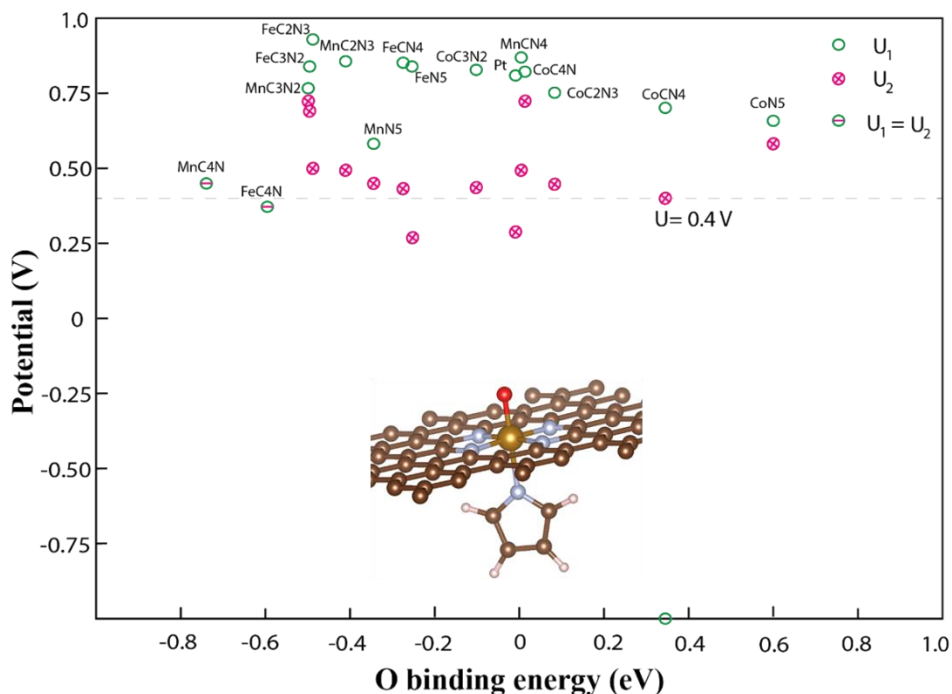


Figure 5 U_1 and U_2 values of ORR process on all possible square-pyramid metal centers are plotted as a function of O binding energy, yielding a high activity plateau region versus a moderate binding energy around 0 eV.

According to these results, most four-coordination moieties are still too strong towards intermediates adsorption, suggesting that the common viewed square-planar structure may not be the true active structure. Therefore, we believe that a further modulation is needed to weaken the adsorption of intermediate species by introducing one another ligand (e.g. pyrrole) to bind on one side of the square-planar moieties to form square-pyramid sites, MC_xN_y ($x+y=5$, as shown in Figure 5), and a ligand binding energy is defined as the reaction energy of the Reaction 3, to determine the possibility of adsorbing an extra ligand (pyrrole) on one side of the moieties. DFT calculations show that all moieties on the strong-binding region are energetically favorable to form

square-pyramid structures, while CoN_4 and weaker binding ones are not (Figure 4). This means Mn, Fe and part of Co based moieties are more likely to exit as square-pyramid structure due to strong adsorption ability. Figure 3 also shows U_1 and U_2 values over these five-coordination active sites, we can find that their O binding energies are drastically reduced, and the catalytic activities are improved. Particularly, FeN_4 -Pyrrole (FeN_5) shows extraordinary promise for ORR catalysis with the highest U_1 value overall, and a relatively low U_2 value for reasonable H_2O_2 inhibiting ability. CoC_2N_2 -Pyrrole (CoC_2N_3) is also improved to a high U_1 value as that of NiC_4 , but its U_2 value is high as well.

3.3 Degradation Analysis

At last, we have investigated the possible degradation of these M-N-C catalysts. Since H_2O_2 production and active sites oxidization and dissociation issue are commonly viewed as the degradation origin,⁴ we use an active oxygen atom to adsorb on the surrounding atoms to simulate the oxidation process. We find that the nitrogen atoms that adjacent to the metal center repulse the oxygen atom, and can be hardly oxidized, which is mainly because of its electronegativity. However, the carbon atoms that bonded to the metal center can be easily oxidized, and the C-M bond is extended (Figure 6), this issue can not only cause strong binding O atoms, but also risks the active moiety dissociation. In this point of view, both NiC_4 and CoC_2N_3 will degrade severely during ORR process, but FeN_5 and CoN_4 have not only excellent

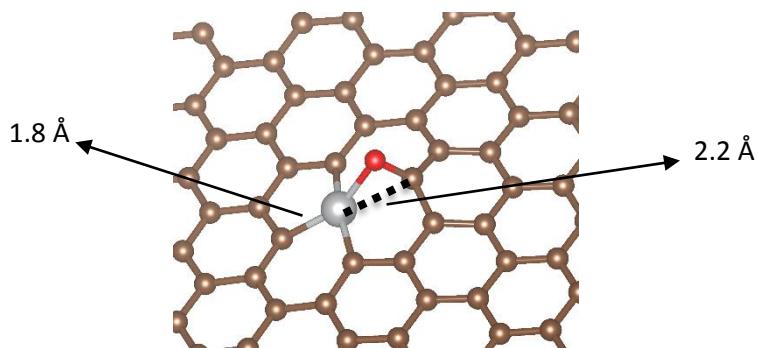


Figure 6 Undesirable O binding configuration on the carbon surrounded active center and leads to possible degradation.

ORR catalytic activity (high U_1 value, low U_2 value), but also better chemical stability attributing to the surrounding nitrogen atoms. In addition, we also calculated the U_1 and U_2 values on the carbon sites that adjacent to nitrogen atoms. These sites function similarly to that on nitrogen-doped graphene (N-G), and their U_1 and U_2 values coincide, about 0.5~0.7 V depending on the nearby nitrogen number, which means that even at a 0.5 V cell potential, all reaction steps in the H_2O_2 production path are still downhill, while that on FeN_5 and CoN_4 are both uphill with at least a 0.3 eV barrier, indicating that for these M-N-C catalysts, carbon sites adjacent to nitrogen atoms are most responsible for the H_2O_2 production, but fortunately, the weak physisorption of O_2 molecule on these carbon sites drastically slow down reaction kinetics.

Chapter 4 Conclusion

In summary, we have demonstrated a fundamental understanding towards the ORR catalytic activity of the biomimetic metal-porphyrin-like moieties, as well as their possible degradation mechanism, based on which we infer that square-pyramid FeN_4 -Pyrrole (FeN_5) and square-planar CoN_4 moieties should have the best performance. Graphene, as a two dimensional carrier material, can well bridge the biological molecule catalysts in living cells with biomimetic electro-catalysts in fuel cells to realize non-precious-metal catalyst design. We believe this work will provide a fundamental support for the future M-N-C catalyst optimization and design.

Bibliography

1. Jasinski, R. *Nature*, **1964**, *201*, 1212.
2. Bashyam, R.; Zelenay, P. *Nature*, **2006**, *443*, 63.
3. Bezerra, C.; Zhang, L.; Lee, K.; Liu, H.; Marques, A.; Marques, E.; Wang, H.; Zhang, J. *Electrochimica Acta*, **2008**, *53*, 4937.
4. Lefèvre, M.; Proietti, E.; Jaouen, F.; Dodelet, J. *Science*, **2009**, *324*, 71.
5. Lee, D.; Lee, W.; Lee, W.; Kim, S.; Kim, Y. *Phys. Rev. Lett.* **2011**, *106*, 175502.
6. Byon, H.; Suntivich, J.; Shao-Horn, Y. *Chem. Mater.* **2011**, *23*, 3421.
7. Li, Y.; Zhou, W.; Wang, H.; Xie, L.; Liang, Y.; Wei, F.; Idrobo, J.; Pennycook, S.; Dai, H. *Nat. Nano.* **2012**, *7*, 394.
8. Chung, H.; Won, J.; Zelenay, P. *Nat. Commun.* **2013**, *4*, 1922.
9. Cao, R.; Thapa, R.; Kim, H.; Xu, X.; Kim, M.; Li, Q.; Park, N.; Liu, M.; Cho, J. *Nat. Commun.* **2013**, *4*, 2076.
10. Nørskov, J.K.; Rossmeisl, J.; Logadottir, A.; Lindqvist, L.; Kitchin, J.; Bligaard, T.; Jónsson, H. *J. Phys. Chem. B*, **2004**, *108*, 17886.
11. Rossmeisl, J.; Logadottir, A.; Nørskov, J.K. *Chem. Phys.* **2005**, *319*, 178.

12. Rossmeisl, J.; Qu, Z.; Zhu, H.; Kroes, G.; Nørskov, J.K. *J. Electroanal. Chem.* **2007**, *607*, 83.
13. Greeley, J.; Stephens, I.; Bondarenko, A.; Johansson, T.; Hansen, H.; Jaramillo, T.; Rossmeisl, J.; Chorkendorff, I.; Nørskov, J.K. *Nat. Chem.* **2009**, *1*, 552.
14. G. Kresse, J. Hafner, *Physical Review B* 1993, *47*, 558–561.
15. G. Kresse, J. Hafner, *Physical Review B* 1994, *49*, 14251–14269.
16. G. Kresse, J. Furthm, *Computational Materials Science* 1996, *6*, 15–50.
17. G. Kresse, J. Furthmüller, *Physical Review B* 1996, *54*, 11169–11186.
18. P.E. Blochl, *Physical Review B* 1994, *50*, 17953–17979.
19. G. Kresse, D. Joubert, *Physical Review B* 1999, *59*, 1758–1775.
20. J.P. Perdew, K. Burke, M. Ernzerhof, *Physical Review Letters* 1996, *77*, 3865–3868.
21. J.P. Perdew, K. Burke, M. Ernzerhof, *Physical Review Letters* 1997, *78*, 1396.
22. Miller, D.; Öberg, H.; Näslund, L.; Anniyev, T.; Ogasawara, H.; Pettersson, L.; Nilsson, A. *J. Chem. Phys.* 2010, *133*, 224701.

23. Niwa, H.; Horiba, K.; Harada, Y.; Oshima, M.; Ikeda, T.; Terakura, K.; Ozaki, J.; Miyata, S. *J. Power Sources*, 2009, 187, 93.
24. Yu, L.; Pan, X.; Cao, X.; Hu, P.; Bao, X. *J. Catal.* 2011, 282, 183.
25. Zheng, Y.; Xiao, W.; Cho, M.; Cho, K. *Chem. Phys. Lett.* 2013, 586, 104.
26. Tripkovic, V.; Skúlason, E.; Siahrostami, S.; Nørskov, J.K.; Rossmeisl, J. *Electrochimica Acta*, 2010, 55, 7975.

초 록

요약하면, 우리는 아래에 서 생체 모방 금속 포르피린 같은 부분의 ORR 촉매 활성뿐만 아니라하는 기반으로 가능한 분해 메커니즘을 향해 근본적인 우리가 유추 증명 평방 피라미드 FeN_5 과 사각형 평면 CoN_4 부분 최고의 성능을 가져야한다. 그래 핀은 이차원 담체 물질로서 잘 비 귀금속 촉매 설계를 실현하는 연료 전지에 전기 - 생체 모방 촉매와 살아있는 세포에 생물 분자 촉매를 해소 할 수있다. 우리는이 작품이 미래의 다국적인 카탈로그 촉매제 최적화 및 설계를위한 기본적인 지원을 제공 할 것으로 판단된다.